UNIVERSITY OF BIRMINGHAM

University of Birmingham
Research at Birmingham

Water promoted photocatalytic Cβ-O bonds hydrogenolysis in lignin model compounds and lignin biomass conversion to aromatic monomers

Shao, Shibo; Wang, Ke; Love, Jason B; Yu, Jialin; Du, Shangfeng; Yue, Zongyan; Fan, Xianfeng

[Link to publication on Research at Birmingham portal](#)

Photocatalytic Selective C-O Bonds Hydrogenolysis and Conversion of Lignin Model Compounds and Lignin Biomass to Aromatic Monomers Using Hydrogen Derived from Water

Shibo Shao[1†], Ke Wang[1†], Jason B. Love[2], Jialin Yu[1], Shangfeng Du[3], Zongyang Yue[1]; Xianfeng Fan[1]*

[1]School of Engineering, The University of Edinburgh, Edinburgh, EH9 3JL, UK

[2]School of Chemistry, The University of Edinburgh, Edinburgh, EH9 3FJ, UK

[3]School of Chemical Engineering, University of Birmingham, Birmingham B15 2TT, UK

†These authors contributed equally to this work.

*Corresponding author: Tel.: +441316505678; Fax: +441316506551; Email: x.fan@ed.ac.uk

Abstract

Lignin biomass is considered as a potential renewable feedstock that can replace fossil resources in the production of aromatic chemicals. The key challenge in its use is selectively cleaving the C-O linkages between natural aromatic units in lignin. In this study, a zinc/sulfur rich phase of zinc indium sulfide (ZIS) photocatalyst was developed for the selective depolymerization of lignin model compounds and kraft lignin biomass under visible light irradiation, with almost quantitative conversion yields of lignin model compounds and over 90% selectivity for the aromatic monomers. In addition, the isotope labelled experiments for the first time proved that water can be used as the hydrogen donor in the photocatalytic hydrogenolysis reaction of C-O bonds instead of less sustainable hydrogen originating from fossil resources (e.g. high pressure H_2 or alcohol). This study shows a promising and environmentally friendly method for converting lignin and lignin model compounds into value-added aromatic monomers.

Introduction

With the increasing awareness of the global crises of climate change and dwindling fossil resources, upgrading conventional chemical industry which remains heavily reliant on fossil resources is a significant challenge. As the only carbon-containing renewable resource, biomass is considered as one of the most promising candidates to replace unsustainable fossil fuel feedstocks in the production of valuable chemicals [1−4]. Among these biomass resources, lignin is the main non-carbohydrate component in lignocellulosic biomass and features complex biopolymer structures comprising of natural functional aromatic monomers generally linked by C−O and C−C bonds [5−8]. Therefore, lignin is deemed as the potential sustainable feedstock to replace fossil fuel resources in the production of valuable aromatic chemicals.

Currently, the transformation of lignin to valuable aromatic chemicals remains a challenge due to its complex structure [1−6]. As shown in Scheme 1, a key problem in the lignin valorization is the effective cleavage of the bonds connecting aromatic units while avoiding dearomatization through hydrogenation of the aromatic rings [6,9]. The C-O bonds, usually represented in the form of β-O-4 linkages, account for over 40% of interunit linkages in lignin structure [3,10,11]. So, the cleavage of these dominant interactions in lignin has been prioritized in methods for lignin depolymerization [6]. However, previous research has been conducted using external hydrogen sources under harsh reaction conditions (e.g. high temperature and high pressure), which can result in dearomatization reactions and undesirable by-products, for example cyclohexanol and benzene (Scheme 1) [1,8,9,11,16]. Furthermore, the external hydrogen donor used in this process is usually high-pressure hydrogen gas or proton derived from alcohols, both of which ultimately originate from fossil fuel resources [8,13−16].

Photocatalytic methods that harness solar energy could be a promising method for selectively cleaving the C-O bonds in lignin model compounds and dioxasolv lignin. For example, a dual light wavelength switching strategy was developed (Pathway 1 in Scheme 1) that can efficiently cleave β-O-4 bonds in

2

lignin model compounds and produce desirable aromatic monomers. This process can be divided into two steps: the oxidation of H-C_α-OH to C=O by Pd-ZnIn$_2$S$_4$ under blue LED light followed by fragmentation and reduction of β-O-4 bonds by TiO$_2$ under UV LED light [17]. Unfortunately, the redundant unused photogenerated electrons or holes had to be consumed by sacrificial agents at each step in order to achieve a high reaction performance. To overcome some of these issues, CdS nanomaterials modified by decorating ultrathin first-row transition metal layer on the surfaces and another zinc indium sulfide photocatalysts were developed that could simultaneously use both photogenerated electrons and holes to efficiently convert lignin model compounds and dioxanesolv poplar lignin to the corresponding aromatic monomers [9,18]. Wu and co-workers developed CdS quantum-dot photocatalysts that could abstract the hydrogen from the hydridic benzylic C_α-H bond and form C_α radical intermediates by photogenerated holes, which decreased the bonding dissociation energy of β-O-4 bonds in lignin model compounds and led to facile fragmentation of β-O-4 bonds to single aromatic products (Pathway 2 in Scheme 1) [5,19]. Moreover, CdS nanoparticles that were surface-modified by Ag$^+$ were also reported to have remarkable photocatalytic activity towards the selective cleavage of β-O-4 bonds to yield aromatic monomers following the same mechanism (Pathway 2 in Scheme 1) [20].
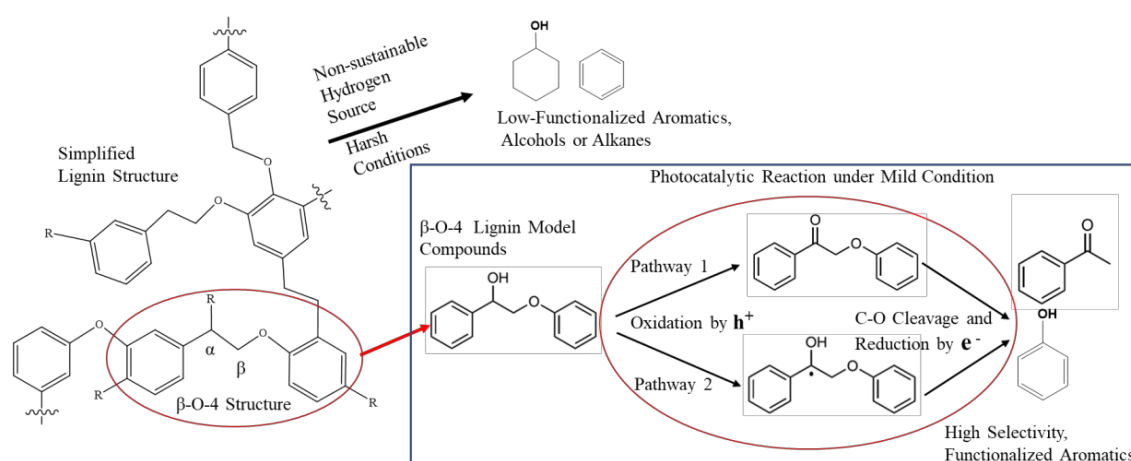
Scheme 1. Simplified lignin structure with various linkages and reported pathways of lignin model compound depolymerization

3

The fragmentation of the C-O linkage could be considered as a combination of oxidation and hydrogenolysis reaction, and photocatalysis could drive this process by providing photogenerated charge carriers. Therefore, C-O bonds could be efficiently cleaved by tuning the photocatalytic properties of the catalysts. Furthermore, the hydrogen source for C-O bonds hydrogenolysis is traditionally either hydrogen gas or an alcohol originating from fossil resources so is another issue that should be addressed. In previous studies of photocatalytic cleavage in lignin model compounds, the solvent without hydrogen-donating property was commonly used and the lignin model compound acted as hydrogen donor for itself [9,20]. The abstracted hydrogen from lignin model compounds could form a "hydrogen pool" and provide hydrogen for hydrogenolysis after the fragmentation of C-O bonds [9,21]. Thus, sufficient active hydrogen on the surface of photocatalysts is essential to facilitate the hydrogenolysis process of C-O bonds and can lead to a better reaction performance.

In this work, a zinc indium sulfide (ZIS) compound with controllable zinc and sulfur composition has been developed through a simple, one-step synthesis and is shown to act as a photocatalyst that can efficiently and completely cleave C-O linkages in lignin model compounds and yield single aromatic monomers with a very high selectivity (~90%). The practicality of this catalyst was also examined by evaluating its activity towards "real" lignin biomass, the unprocessed by-product waste of kraft lignin from a local paper industry. It should be noted that this process operates under very mild conditions and also without using H_2, alcohols or other unsustainable hydrogen sources. More importantly, based on the results from isotope labelled experiments, water, for the first time, has been proven its potential to be the hydrogen donor for the photocatalytic hydrogenolysis reaction of C-O bonds and is therefore sustainable. The mechanism of C-O bonds fragmentation and the hydrogen transfer route in the hydrogenation process was also investigated in this work. Thus, this study reveals the great potential of photocatalysis in utilization of lignin biomass as the feedstock to produce value-added aromatic chemicals via a green and economic method.

EXPERIMENTAL SECTION

Materials

4

All the chemical reagents used for the synthesis of catalysts were analytic grade and used as received without further purification. $Zn(NO_3)_2 \cdot 6H_2O$ (98%), $InCl_3$ (anhydrous, 99.99%), thioacetamide (99%+) and acetonitrile were purchased from Fisher Scientific International, Inc. Cetyltrimethylammonium bromide (CTAB, >99%), all photogenerated charged carriers scavengers and radical capture agents were purchased from Sigma-Aldrich Co., Ltd. 2-Phenoxy-1-phenylethanol (PP-ol) and 2-phenoxyacetophenone (PP-one) were purchased from Fluorochem Ltd. Kraft lignin was obtained from a local paper factory and processed from corn stalk. Deionized (DI) water was produced using a CENTRA® R200 Centralized Purification and Distribution Systems.

Preparation of Catalysts

The synthesis in this work was modified from the $ZnIn_2S_4$ nanomaterials synthesis in the literature. [22] A certain amount (x mmol, x=1.5, 3.0, 4.5, 6.0, 7.5) of $Zn(NO_3)_2 \cdot 6H_2O$, and $InCl_3$ (663.5mg, 3.0 mmol) were dissolved in 50 mL of DI water in a 100 mL beaker, then CTAB (364.5 mg, 1mmol)was added to the solution. Next, the solution was magnetically stirred for 30 min at room temperature before adding thioacetamide (y mmol, y=12, 15, 18, 21, 24). The mixture was poured into a 100 mL stainless Teflon-lined autoclave reactor after being stirred for another 30 min, then securely sealed, and placed in an oven heating for 16 h. The heating temperature was 160 °C with a 4 °C/min of heating ramping. After heating, the autoclave was taken out from the oven and naturally cooled down. The yellow sediment at the bottom after centrifugation was collected, then rinsed with 50 mL absolute ethanol and 75% ethanol /water mixture for 5 times respectively. The powder was further dried under vacuum at 60 °C for 12 h. Based on the molar ratio of the added precursors of $Zn(NO_3)_2 \cdot 6H_2O$ in the above reactions, the obtained products were labelled as ZIS-1, ZIS-2, ZIS-3, ZIS-4 and ZIS-5.

Photocatalytic Reaction Experiments

A customized quartz reactor with cooling water jacket was used in this work. The light source used in the experiment was a xenon arc lamp (manufactured by Perfect Light Company) equipped with a PE300BF type light bulb and a 420 nm UV filter. The lamp was set up at a fixed position to ensure the light intensity in different tests were same, which was about $0.35W/cm^2$ at the center. Typically, 10mg of catalyst, 10 mg of lignin model compounds (or 100 mg kraft lignin biomass) and 5 mL of solvent

5

(CH$_3$CN or CH$_3$CN/H$_2$O mixture) were added into the reactor. The mixture formed a well-dispersed suspension with the aid of magnetic stirring. After deaeration by nitrogen or other gas (including argon and oxygen), the reactor was tightly sealed and placed under illumination with magnetic stirring at 500 rpm. The temperature was kept at 20 °C with the aid of the cooling water system. After the reaction, the catalyst was removed by centrifugation (10000 rpm for 10 min). Then, 4 mg methylparaben was added into 1 mL supernatant liquid as the internal standard in each test and diluted by a factor of 50 times with acetonitrile. The conversion of lignin model compounds and the yields of aromatic monomer products were identified and quantified by gas chromatography/ mass spectrometry (GC/MS, QP2010 SE, Shimadzu). The following operation parameters were applied to the GC-MS: injection temperature, 280 °C; column temperature program: 80 °C for 2 min, then increasing the temperature to 270 °C at a rate of 10 °C/min, then heat up to 300 °C at a rate of 30 °C/min and holding the temperature for 5 min, The scanning speed of MS is 1000, start from 45 m/z and end at 220 m/z.

Materials Characterization

XRD analysis was carried out using a Bruker Phaser-D2 diffractometer with Cu Kα X-ray source at the voltage of 40 kV and current of 40 mA. The morphologies and structures of materials were imaged by scanning electron microscopy with Energy Dispersive X-Ray Spectroscopy function (SEM-EDS, Zeiss Sigma VP) and transmission electron microscopy (TEM, JEOL JEM-2100F) respectively. The BET surface area of each material was measured by a Quantachrome IQ sorption analyzer with N$_2$ at 77 K. The light absorption property and band gap of each prepared material were analyzed by UV/Vis Diffuse Reflectance Spectroscopy (DRS) on a JASCO V-670 spectrophotometer equipped with an integration sphere in the spectral range of 200–900 nm and BaSO$_4$ was used as the reflectance standard. The chemical states of each element in prepared samples and X-ray photoelectron valence band spectra (XPS-VB) were characterized on an X-ray photoelectron spectrometer (ThermoFisher K-Alpha) with an Al Kα X-ray source. The composition of each prepared catalysts was determined by EDS and inductively coupled plasma optical emission spectroscopy (ICP-OES, Varian Vista Pro). The photocurrent response spectroscopy measurements were carried out at a constant potential of 0.2 V to

the working electrode and a 300W Xe lamp with a UV filter which was also used as the light source during the experiments.

Results and Discussion

Inductively coupled plasma optical emission spectroscopy (ICP-OES) was first used to determine the elemental compositions of all samples. As shown in Table 1, the ratio of In/Zn and S/Zn in ZIS-1 are very close to the atomic ratio of each element in pristine $ZnIn_2S_4$, and it is clear that the composition of indium and sulfide decreased with the increasing the amount of zinc and sulfide precursors added in catalyst synthesizing stage. These results indicate that the additional zinc and sulfide have been successfully introduced into the synthesized materials.

Table 1. The elemental composition determined by ICP-OES (normalized respect to Zinc)

ICP-OES	ZIS-1	ZIS-2	ZIS-3	ZIS-4	ZIS-5
In/Zn(atomic%)	2.176	0.964	0.828	0.588	0.586
S/Zn(atomic%)	3.807	2.139	2.109	1.712	1.676

The crystal structures and phases of the prepared materials in this study were determined by XRD analysis. As shown in Figure 1, the distinct peaks of ZIS-1 at about 21.6°, 27.7°, 30.4° and 47.2° correspond well to the diffraction of the (006), (102), (104) and (110) crystal planes in the standard hexagonal Zinc Indium Sulfide crystals (JCPDS 03-065-2023), indicating that zinc indium sulfide was successfully synthesized [22,23]. These peaks are also seen in the samples containing higher zinc and indium sulfur compositions, which is consistent with the XRD pattern of zinc and sulfur rich phase of zinc indium sulfide previously reported [24,25]. The peak (006) shifts to the lower degree has also been reported due to the use of CTAB as the surfactant in synthesis process [22,25,26]. The additional zinc and sulfur contents in zinc indium sulfide generally form atomic layer structures arranging in a repeated sequence of S-Zn-S-In-S-Zn-S along the c-axis [24]. In addition, with the assistance of CTAB surfactant and hydrothermal synthetic process, the crystal of zinc indium sulfide grew up in a 2D structure, which resulting in the peaks at 39.8°, 45.7°, and 52.2° from the XRD pattern of standard zinc indium sulfide are not discernible in all prepared samples [22,26,27]. The formation of 2D flexible layer-structure in

7

samples has been reported previously to be favorable for photocatalytic activity by enhancing the separation of photoexcited electron-hole pairs [27]. Furthermore, with increasing amounts of zinc and sulfur precursors during synthesis stage, new peaks located at 28.55°, 47.51° and 56.29° are seen in the XRD patterns of ZIS-3, ZIS-4 and ZIS-5, which are indexed to the diffraction of the (111), (220) and (311) crystal planes from the standard cubic ZnS crystals (JCPDS 00-005-0566). These results indicate that the additional zinc ions have reacted with the sulfur from excess thioacetamide to form zinc sulfide; the intensity of the peaks corresponding to ZnS became significantly higher and sharper with increasing the amount of zinc and sulfur precursors during the synthesis. In contrast, the diffraction peaks associating with the ZnS can be barely seen in ZIS-2, even though the ICP-OES analysis indicated higher zinc and sulfur composition in ZIS-2 than in the stoichiometric $ZnIn_2S_4$. Also, no obvious shift of peaks in XRD pattern could be observed with increasing zinc and sulfur composition from ZIS-1 to ZIS-5, which indicates that zinc or sulfur are not dopants in these samples. Thus, it is likely that the additional zinc and sulfur form a zinc and sulfur rich phase of zinc indium sulfide, and ZnS in sample ZIS-3, 4, 5 were formed by excess zinc and sulfur.
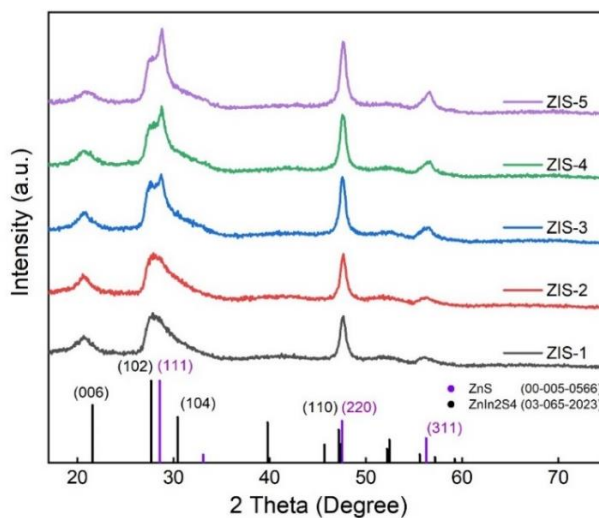

Figure 1. Powder X-ray diffraction (XRD) patterns of ZIS samples

Table 2. The results of elemental analysis by SEM-EDS

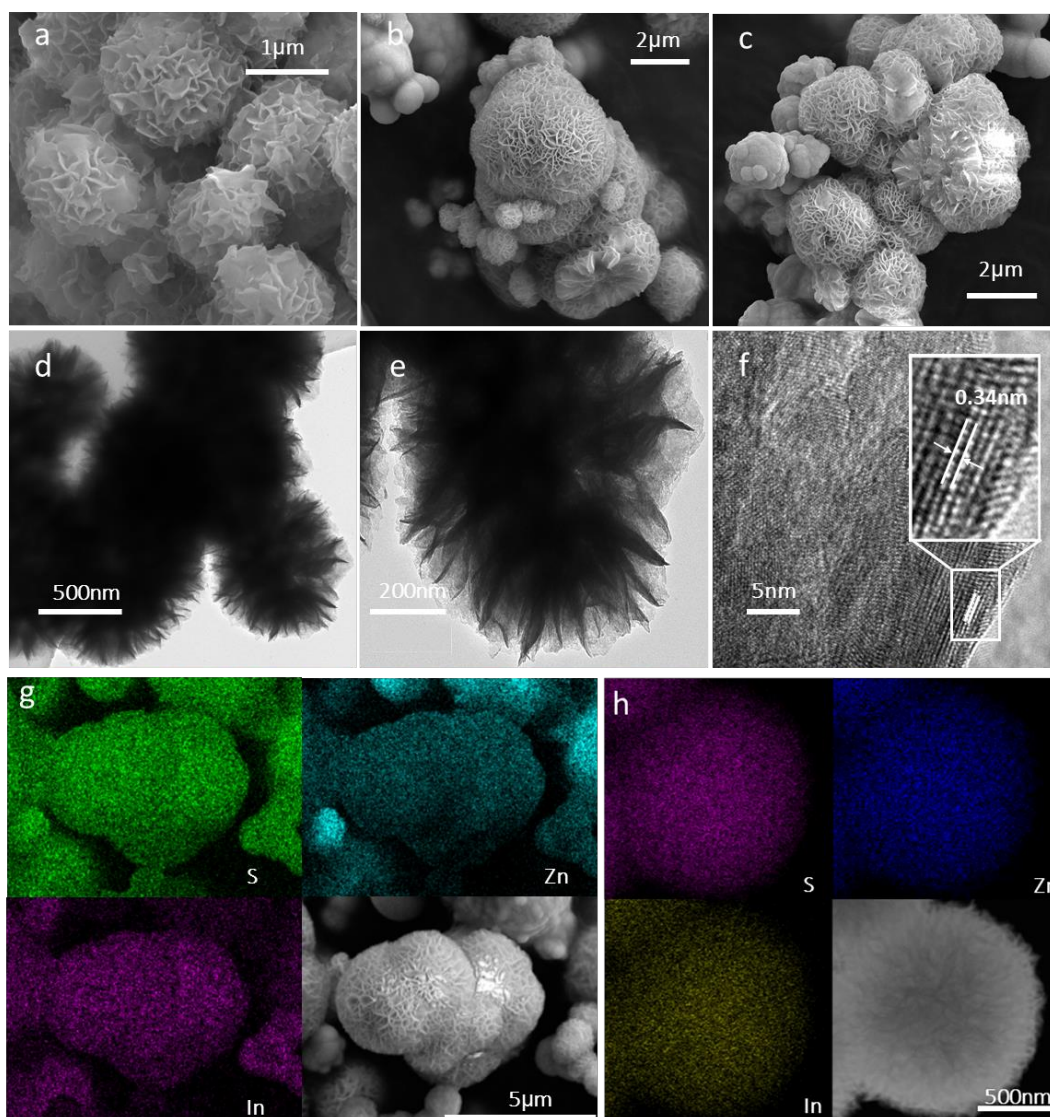|	"Hydrangea" Part (Zinc Indium Sulfide)		"Solid Microsphere" Part (Zinc Sulfide)	
Sample ID	In/Zn (atomic ratio)	S/Zn (atomic ratio)	In/Zn (atomic ratio)	S/Zn (atomic ratio)
ZIS-1	2.070	3.943	-	-
ZIS-2	1.430	2.871	-	-
ZIS-3	1.228	2.612	0.085	1.035
ZIS-4	1.224	2.487	0.071	1.031
ZIS-5	1.235	2.643	0.064	1.034

Figure 2. SEM image of (a) ZIS-1, (b) ZIS-3, (c) ZIS-5; TEM image of ZIS-3 with different magnifications (d-f); Element mapping of ZIS-3 by (g) SEM and (h) TEM with different magnifications

Scanning electron microscopy (SEM) and transmission electron microscopy (TEM) were used to further investigate the microstructure and components of the catalysts. It has been reported that zinc indium sulfide nanolayers are prone to aggregate with each other during the hydrothermal process [26,27]. As can be seen in Figure 2(a), due to the effect of surfactant and hydrothermal condition, $ZnIn_2S_4$ crystallites have self-organized into microspheres and form a hydrangea-like structure in sample ZIS-1; this hydrangea-like microsphere was observed in all samples. The TEM images of ZIS-3 (Figure 2(d) and (e)) also demonstrate that the samples are composed of relatively uniform hydrangea-like microspheres with slight aggregation which agrees with the SEM results. Each microsphere is formed by numerous very thin layers with the size of approximately 100-200nm. Also, no discontinued crystal fringes could be observed on the zinc indium sulfide petals from HRTEM image (Figure 2(f)), indicating good crystalline structures of the materials formed. The interplanar spacing of ZIS-3 was measured to be 0.34 nm, which is slightly wider than the distinct (102) planes of pristine $ZnIn_2S_4$, maybe owing to the rich compositions of zinc and sulfur in zinc indium sulfide [28]. In addition, a different form of solid microspheres was observed of which the amount gradually increased with increasing zinc and sulfur composition, which also accords with the XRD analysis with the characteristic XRD peaks of ZnS becoming higher and sharper in sample ZIS-3, ZIS-4, and ZIS-5. (Figure 2(b) and (c); Figure S1-S3 in Supplement) Therefore, elemental imaging was employed to determine the elemental composition at different parts of structure in ZIS-3 to further identity the component of these samples. As shown in Figure 2(g) and (h), zinc, indium, and sulfur are dispersed very uniformly on the hydrangea-like microsphere area whereas the signal intensity of indium is very weak on the solid microsphere. Selected small areas on the hydrangea-like microsphere part of samples and solid microsphere part of samples were selected to be characterized by SEM-EDS respectively (Table 2), which reveals that the Zn/S ratio on the solid microspheres is very close to 1 along with very low In/S ratio, which further supports the presence of ZnS [23]. It should be noted that the elemental ratio of Zn, In and S on the petal of zinc indium sulfide also varied from around 1:2:4 in ZIS-1 and to around 1:1.2:2.5 in ZIS-3,4,5 even though these samples contain higher zinc and sulfur composition. These data indicate that there is a saturated concentration for additional zinc and sulfur composition in the

10

zinc indium sulfide structures using the current synthetic method and that excess zinc and sulfur will form solid microspheres of ZnS instead of forming zinc and sulfur rich phases of zinc indium sulfide.
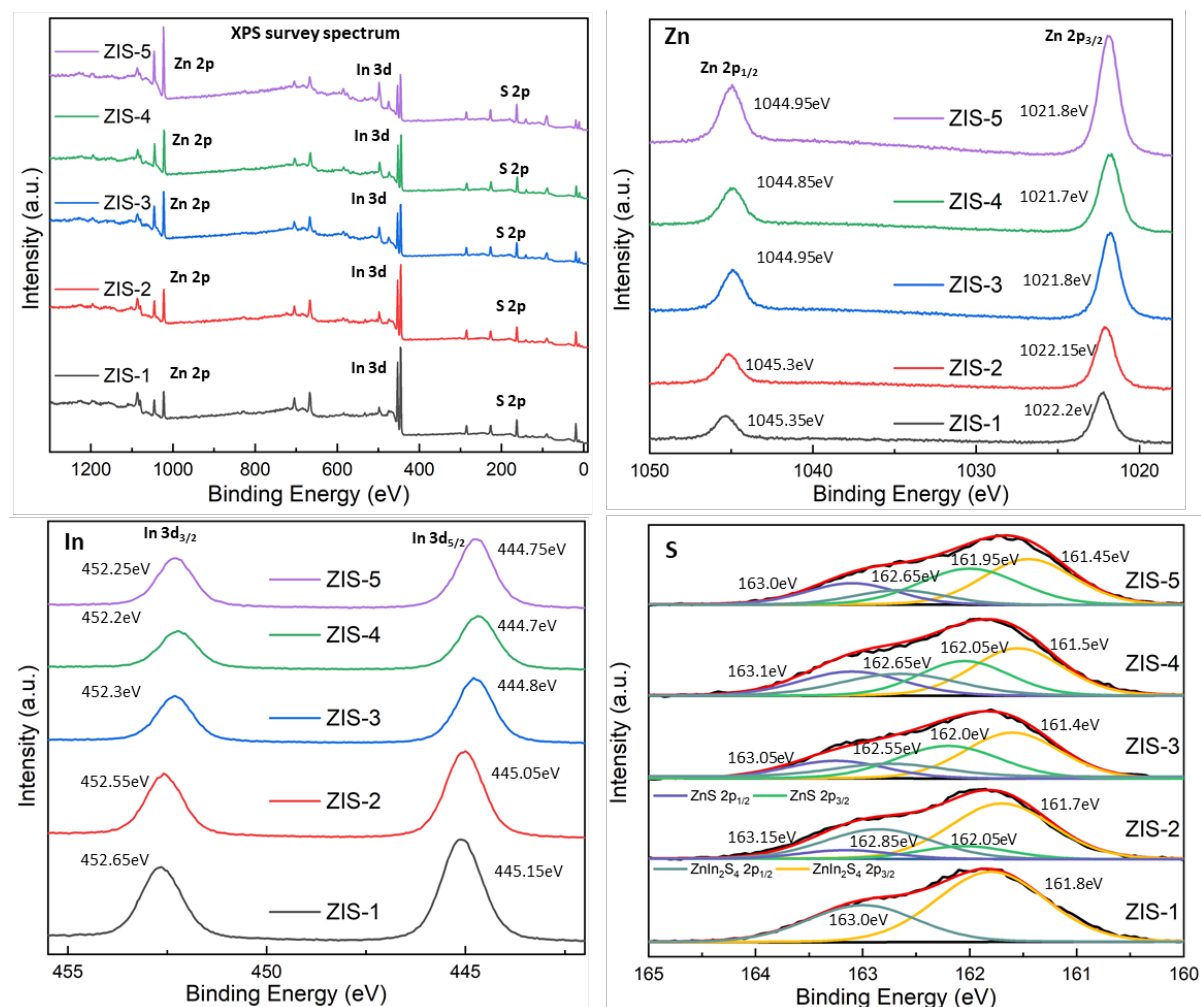

Figure 3. XPS survey spectrum and XPS spectra of Zn 2p, In 3d and S2p.

X-ray photoelectron spectroscopy (XPS) was employed to analyze the elemental composition and valence state on the surface of each sample. All spectra were referenced to C 1s peak at of 284.8 eV arising from adventitious carbon and the positions of each peaks are stated respectively in Figure 3 [29]. The XPS survey spectra and high-resolution XPS spectra for each element confirm that zinc, indium and sulfur coexist in each sample. For pristine $ZnIn_2S_4$ in ZIS-1, the binding energies of Zn 2p, In 3d and S 2p peaks are very close to those reported in the literature [30]. The S 2p peak in the XPS spectra of ZIS-2, 3 ,4 and 5 were deconvoluted into two sets of peaks, suggesting that S^{2-} in these samples are

11

in different chemical environments, most likely ZnS and zinc indium sulfide [31]. In addition, negative shifts of peaks are observed for every element with increasing zinc composition from ZIS-1 to ZIS-3. It is because the electronegativity of Zn is lower than other elements in the materials, which increases their local electron density and decreases the binding energy. No obvious additional binding energy shift was observed for Zn 2p, In 3d and S 2p traversing from ZIS-3 to ZIS-4 and ZIS-5 that have increasing zinc and sulfur compositions, which agrees with the previous elemental analysis results that excess amount of zinc and sulfur cannot enter the crystal structure of zinc indium sulfide instead form independent ZnS in the samples.
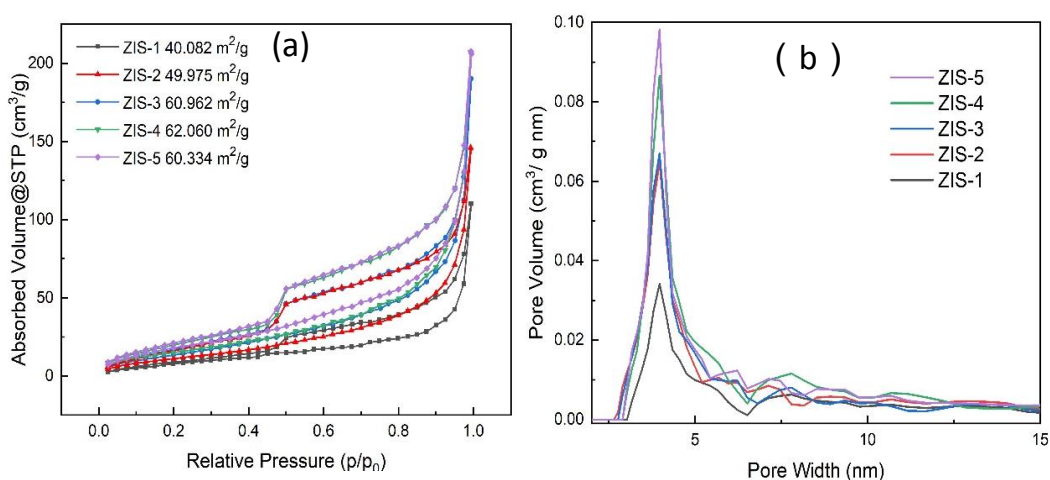

Figure 4. (a) Nitrogen adsorption/desorption isotherms (77 K) with BET specific surface areas and (b) pore size distribution curves of ZIS samples

Specific surface area and pore structure are also critical factors greatly affecting the catalytic property of catalysts. As shown in Figure 4, the isotherms for all samples could be identified as type IV with hysteresis loops, suggesting the presence of well-structured mesopores in the samples [32,33]. With increasing of zinc and sulfur components in the materials, the BET surface area of samples ZIS-1, 2 ,3 gradually increased from 40.082 m^2/g to 60.963 m^2/g, which could provide more active sites and improve the catalytic activity during the reaction. However, it should be noticed that further increasing the zinc and sulfur composition in the samples had no obvious effect on the specific surface area after ZIS-3, maybe owing to the competition between the formation of $ZnIn_2S_4$ and ZnS during the single-

12

pot hydrothermal synthesizing process [33]. Also, the main pore sizes of the synthesized zinc indium sulfides are all in a range of 3-5 nm, which is similar to the literatures [33,34].

Photocatalytic Cleavage of β-O-4 Lignin Model Compound

As the main C-O form in lignin, the light-driven β-O-4 bond cleavage was tested by all catalysts in this study. 2-phenoxy-1-phenylethanol (PP-ol) was employed as the lignin model compound to evaluate catalytic performance due to its signature C_β-O structure and its ready comparison to previously published works [9,15,18,20,21,35–37]. The results of first 2 entries in Table 3 reveal that PP-ol can barely be converted or decomposed without catalyst under visible light irradiation or with catalyst under dark conditions. When pristine $ZnIn_2S_4$ (ZIS-1) was used as the photocatalyst, 88.1% of PP-ol was converted with 34.5% of reacted PP-ol oxidized to the undesirable by-product 2-phenoxyacetophenone (PP-one) instead of single aromatic products. Upon increasing of the zinc and sulfur composition, the photocatalytic reaction performance and selectivity could be improved remarkably as shown in Figure 5(b). After 1.5 h of visible light irradiation, catalysts ZIS-2, ZIS-3, ZIS-4 completely converted PP-ol into aromatic monomers with ZIS-3 showing the best selectivity: over 90% of PP-ol was converted to aromatic monomers (phenol and acetophenone) with less than 10% PP-ol converting to PP-one. This result indicates that the photocatalytic performance of zinc indium sulfide photocatalysts could be improved by rich composition of zinc and sulfur. Further, it should be noticed that the selectivity of ZIS-4 and the reaction performance of ZIS-5 were lower than ZIS-3. It is very likely that this decreasing catalytic performance is caused by an excessive amount of ZnS which could be visually observed from SEM images in the catalysts. ZnS has been reported to relatively inert towards visible light excitation due to its wide band gap and is therefore an inactive photocatalysts for this reaction [20].
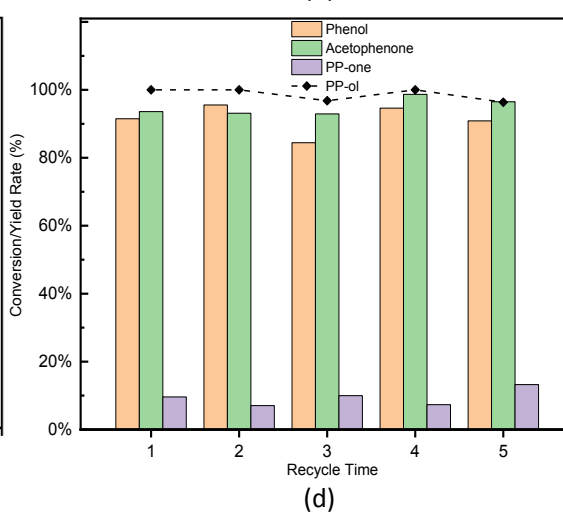
13
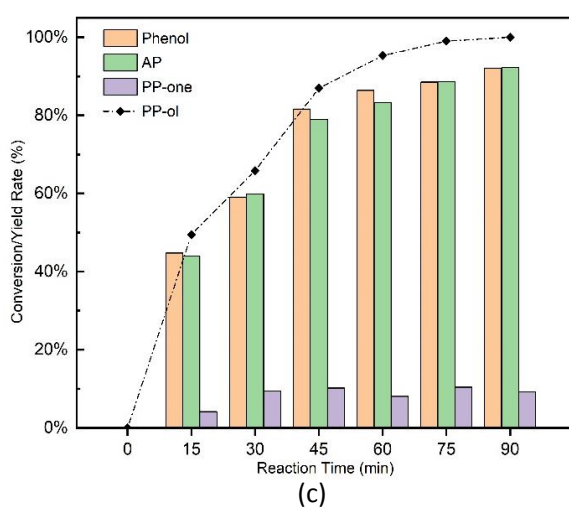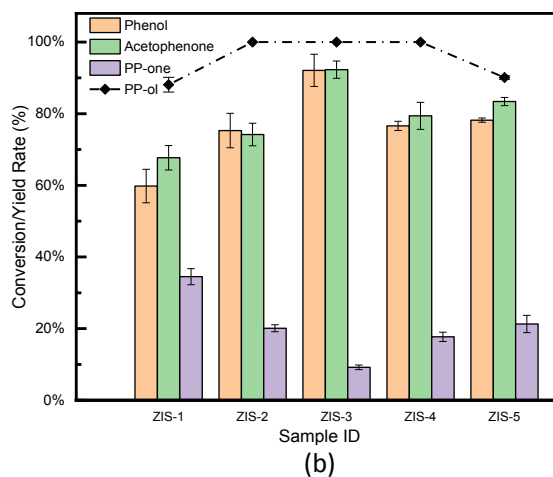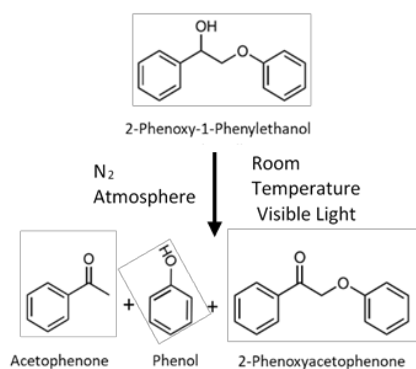
Figure 5. (a) Graphic summary of photocatalytic reaction of PP-ol; (b) Conversion and product yields with each sample; (c) variation in the reaction time of ZIS-3; (d) Reusability test for ZIS-3. Typical reaction condition: 10mg of PP-ol, 10 mg of catalyst, 5mL of solvent (CH$_3$CN:H$_2$O=2:3), visible light irradiation (0.35W/cm^2), Room temperature (20-25 °C), 90min. The quantitative analysis of each chemical was determined by GC-MS with Methylparaben as the internal standard.

$$Conversion\% \ (Reactant) = 1 - \left(\frac{Residual \ Reactant}{Initial \ Reactant}\right); \quad Yield\% \ (Product) = \frac{Mole \ of \ Product \ Formed}{Mole \ of \ Reactan \ Converted} \times Conversion\%$$

Table 3. Screening of various Reaction Conditions for the Fragmentation of Lignin Model Compounds

Entry	Catalyst	Reaction Condition Variables	Conversion%	Selectivity%		
			PP-ol	Phenol	Acetophenone	PP-one
1	No Catalyst	-	~0%	~0%	~0%	~0%
2	ZIS-3	Dark	~0%	~0%	~0%	~0%
3	ZIS-3	Nitrogen	~100%	91.2%	91.7%	8.2%
4	ZIS-3	Argon	~100%	93.7%	91.9%	4.7%
5	ZIS-3	Air	90.7%	9.4%	3.6%	91.4%
6	ZIS-3	Oxygen	82.3%	7.7%	4.3%	93.1%
7	No Catalyst	PP-one as reactant	-	~0%	~0%	~0%
8	ZIS-3	PP-one as reactant	-	~0%	~0%	3.6%
9	ZIS-3	CH_3CN	63.8%	33.6%	34.4%	53.1%
10	ZIS-3	H_2O:CH_3CN =1:4	71.0%	50.8%	47.7%	36.9%
11	ZIS-3	H_2O:CH_3CN =2:3	83.6%	68.1%	69.8%	30.9%
12	ZIS-3	H_2O:CH_3CN =3:2	~100%	91.2%	91.7%	8.2%
13	ZIS-3	H_2O:CH_3CN =4:1	~100%	66.1%	79.3%	4.1%
14	ZIS-3	EtOH:CH_3CN =3:2	46.4%	36.3%	30.6%	59.8%

Typical reaction condition: 10mg of PP-ol, 10 mg of catalyst, 5mL of solvent (CH_3CN:H_2O=2:3), visible light irradiation (0.35W/cm^2), Room temperature (20-25 °C), 90min. The quantitative analysis of each chemical was determined by GC-MS with Methylparaben as the internal standard.

$$Conversion\% \ (Reactant) = 1 - (\frac{Residual\ Reactant}{Initial\ Reactant}); Selectivity\% \ (Product) = \frac{Mole\ of\ Product\ Formed}{Mole\ of\ Reactant\ Converted}$$

The reaction kinetics of ZIS-3 were also evaluated (As shown in Figure 5(c)). Within the first 15 min of illumination, almost half of PP-ol was converted with 90% selectivity for the desired single aromatic products (Acetophenone and Phenol). As the reaction was conducted in a batch reactor system, the reaction rate decreased gradually because of the decreasing concentration of reactant, and full conversion of PP-ol was achieved after only 90 min of illumination. The selectivity of single aromatic products was maintained over 90% while the transformation to PP-one was remained at a relatively low level during the entire reaction process. Comparing this result with entries 7 and 8 in Table 3, it is clear that the reaction mechanism is different to that reported in the literature. In the latter cases, PP-ol is oxidized to the ketone PP-one which then decomposes to single aromatic monomers, whereas for ZIS-3 in this study, PP-ol is converted to acetophenone and phenol without PP-one as an intermediate

15

product; instead, the conversion of PP-ol to PP-one is a side-reaction which has a negative effect to the targeted C-O bond fragment in this study [38,39].

Additionally, it is very critical for a heterogeneous catalyst to have a good reusability for practical applications. In this study, the heterogeneous catalysts ZIS-3 could be straightforwardly separated after the reaction by filtration or centrifuge. After washing by ethanol and water to remove residual adsorbed chemicals on the surface of catalysts and drying under vacuum, over 85% amount of the catalyst could be collected for reuse. The recycling experiment of ZIS-3 catalyst was studied for 5 cycle times under identical reaction conditions, with no obvious drop of catalytic performance including conversion rate of PP-ol and the selectivity for aromatic monomers (Figure 5(d)). Furthermore, the recycled catalysts were characterized by XRD and ICP-OES and no clear differences were observed from the characterization of pristine ZIS-3 (Figure S4 and Table S1 in Supplement).

It has been also found that the reaction atmosphere is also an important parameter which can significantly influence the PP-ol conversion. The results of entry 3 and 4 in Table 3 show that completely conversion of PP-ol with high selectivity towards single aromatic monomers can be achieved when the reactions were performed under inert gas atmosphere (nitrogen and argon). However, the reaction performance decreased dramatically when the reactions were carried out under air or pure oxygen, with the oxidation of PP-ol to PP-one significantly promoted and the desired C-O bonds fragmentation reaction suppressed to less than 10% (entry 5 and 6 in Table 3). Besides the oxidative role of oxygen, another possible reason could also be that oxygen can capture the photoexcited protons and photogenerated electrons thus suppressed the fragment of C-O bonds and decreased the photocatalytic performance [9,40]. These results recommend that this reaction should be performed in an anaerobic environment to avoid undesired oxidative transformation of PP-ol to its corresponding ketone PP-one.

While previous studies used hydrogen gas or alcohol as hydrogen donors in the reaction, in this work, water was employed as a sustainable hydrogen source [1,16,41]. Different amounts of water were introduced into the reaction system to investigate the effect of water to the reaction (entry 9-13 in Table 3). Increasing the water/acetonitrile ratio from 0 to 3:2 resulted in an increase in the conversion of PP-

16

ol from 63.8% to almost 100% along with an increase in the selectivity of desired aromatic monomer from about 30% to over 90%; additionally, the selectivity of by-product of PP-one decreased from 53.1% to 8.2%. These results clearly show that the pronounced promotion effects of water on the PP-ol conversion to corresponding aromatic monomers. However, the presence of excess water in the reaction system has a negative effect due to the low solubility of lignin model compounds in water (entry 13) [9,18]. Ethanol was also tested as the hydrogen donor, but in contrast with the previous works, it is found that the reaction performance deteriorated when ethanol was used (entry 14 in Table 3) [9]. A potential reason could be that ethanol can also act as a scavenger for photogenerated holes and therefore suppressed the photochemical reaction. Moreover, it has been reported that the great solubility of PP-ol and PP-one in the mixture of CH_3CN and ethanol could also increase the selectivity for PP-one [18].

After testing with different lignin model compounds, ZIS-3 catalyst was further applied to catalyze the fragmentation of kraft lignin under visible light. The products in the solution were analyzed and identified by a GC-MS and a controlled experiment without catalysts was also conducted under same condition for comparation (Figure S5 in Supplement). After 16 h of illumination, the differences between the reaction with catalysts and without catalysts are clear: the quantities of various aromatic monomers are significantly increased with catalyzing by ZIS-3. This result implies that the photocatalysts developed in this study could be deployable for lignin valorization through its conversion into valuable aromatic monomers.

Mechanism for C-O bond cleavage

To further understand the reaction mechanism of C-O fragmentation in the reactions, a series of control experiments were performed. In order to investigate the mechanism of photogenerated charge carriers in the reactions, hole scavengers (Na_2S and Na_2SO_3) and an electron scavenger ($Na_2S_2O_8$) were respectively introduced to the reaction system and the results were shown as entry 1 and 2 in Table 4. The hole scavenger almost halved the conversion of PP-ol and extremely suppressed the formation of PP-one due to the effect of the scavenging of photogenerated holes. This result agrees with previous studies and indicates that the photogenerated hole can oxidize PP-ol to PP-one, and transform PP-ol to radical intermediates which are essential for the following C-O bond fragmentation [9,18,20]. In

17

contrast, the reaction with added electron scavenger could still convert almost 100% of PP-ol but with an obvious decrease in the selectivity for the desired aromatic monomers, suggesting that the photogenerated electrons are important to the C-O bonds fragmentation and the following hydrogenolysis process [5,9,20]. Also, when the photogenerated holes and electrons were consumed by corresponding scavengers, more photogenerated electrons or holes could escape from the recombination of photogenerated charge carriers, which respectively results in decreasing or increasing the PP-one yield. These phenomena reveal that both photogenerated electrons and holes were participating in the reaction. Moreover, previous literature has determined that water can also interact with the photocatalysts and form hydroxyl radicals which are highly oxidative [43]. Thus, D-mannitol was employed as a hydroxyl radical scavenger to evaluate the effect of hydroxyl radicals in this reaction. As shown in Entry 3 in Table 4, the result shows that the quenching of hydroxyl radicals had negligible influence on reaction performance, which agrees with previous works claimed that the photogenerated holes probably can directly interact with PP-ol adsorbed on the surface of photocatalysts [20,42–44]. Nevertheless, it has also been reported that hydroxyl radicals can oxidize the abstract hydrogen from benzyl alcohol, so the possibility that the hydroxyl radicals may also react with PP-ol and form radical intermediate cannot be ruled out [45].

Table 4. Control experiments catalyzed by ZIS-3 with different additives

Entry	Reaction Condition Variables	Conversion%		Selectivity%	
		PP-ol	Phenol	Acetophenone	PP-one
1	Hole scavenger	51.9%	93.0%	87.9%	~0%
2	Electron scavenger	~100%	67.5%	74.2%	25.7%
3	Hydroxyl radical scavenger	~100%	86.2%	84.5%	13.5%
4	Radical scavenger	59.7%	31.3%	23.7%	44.2%

Reaction condition: 10 mg of PP-ol, 10 mg of catalyst, 5 mL of solvent ($CH_3CN:H_2O = 2:3$), visible light irradiation (0.35 W/cm^2), room temperature (20-25 °C), 90min. The hole scavengers used were 20 mg Na_2S and 10 mg Na_2SO_3; the electron scavenger used was 30 mg $Na_2S_2O_8$; •OH* scavenger used was 50mg of D-mannitol; the radical scavenger used was 30 mg 5,5-dimethyl-1-pyrroline-N-oxide (DMPO). The quantitative analysis of each chemical was determined by GC-MS with methylparaben as the internal standard.

18

The light absorption and energy band positions have always been considered as the key factors in photocatalysis. As shown in diffuse reflectance UV-Vis spectroscopy (DRS) plots (Figure 6(a, b)), the adsorption edges of samples with higher zinc and sulfur components shift to a shorter wavelength. This blue-shift of absorption could be attributed to the existence of ZnS which has a wide band gap (around 3.5eV) [46]. It should be noted that the most efficient catalyst, ZIS-3, still has a strong light adsorption in visible light region while ZIS-4 and ZIS-5 show a clear decrease of adsorption in the visible region, which can perhaps explain the decrease in catalytic performance of ZIS-4 and ZIS-5. To further understand the relationship between the photocatalytic reaction performance and composition of catalysts, the band edge positions of each sample were determined by a combined analysis of modified Kubelka–Munk plot and XPS-VB spectra and summarized in Table 5. The band gap of the catalysts increased from 2.23eV to 2.62eV while the valence band maximum (VBM) increased from 1.54 eV to 1.85 eV upon increasing of zinc and sulfur components, thus, the conduction band maximum (CBM) could be calculated based on the formula of $E_{CB} = E_{VB} - E_{Bandgap}$, and varies from −0.69 eV to −0.81 eV [47]. Generally, a more positive VB represents a stronger oxidization property while a more negative CB represents a better reduction ability [21]. In this study, it has been confirmed that the C-O cleavage process involves both oxidation and reduction reactions driven by photogenerated holes and electrons respectively. Also, increased amounts of zinc and sulfur components in the catalysts significantly affected the band edge alignment of samples, therefore, directly impacted upon the catalytic performance. Compared with the other ZIS samples, ZIS-3 is the most efficient photocatalyst and exhibits an appropriate band gap for visible light excitation and optimized VBM and CBM edges, which leads to better photocatalytic activity with excitation by visible light [20].

Table. 5 Band alignment of each sample

	Band gap (eV)	VB (eV)	CB (eV)
ZIS-1	2.23	1.54	-0.69
ZIS-2	2.32	1.62	-0.70
ZIS-3	2.48	1.75	-0.73
ZIS-4	2.57	1.79	-0.78
ZIS-5	2.66	1.85	-0.81

Since both photogenerated electrons and holes have been proven to be important to this reaction, the transient photocurrent response of each sample was examined to evaluate the efficiency of photoexcited electron/hole generation and transportation. Although ZIS-1 (pristine $ZnIn_2S_4$) has the lowest band gap, all of the modified materials with additional zinc and sulfide components display higher photocurrent responses (Figure 6(c)), which shows that the rich zinc and sulfur composition in ZIS-2~5 can efficiently enhance the migration of photo-charge carriers and inhibit the recombination of photoexcited electron-hole pairs [30]. As expected, ZIS-3 with the highest catalytic activity in this study also shows the highest photocurrent under visible light illumination, further revealing that it can provide a greater amount of effective photoinduced charge carriers and facilitate the C-O bond cleavage [30,48]. The significant decrease in photocurrent response from ZIS-4 to ZIS-5 could be attributed to the wide band gap.
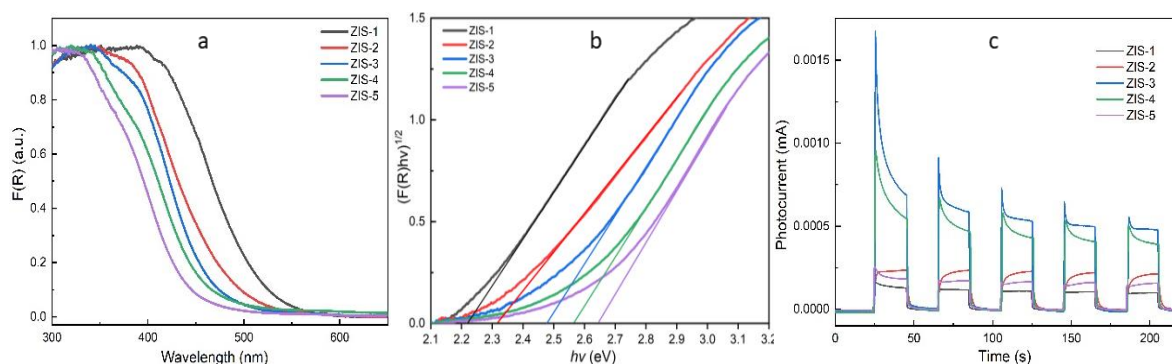

Figure 6. (a)Diffuse reflectance UV/Vis spectra, (b) the corresponding plots of modified Kubelka–Munk function versus the energy of exciting light, (c)Transient photocurrent responses of each sample

In this study, it has been confirmed that properly increasing water content in the reaction system can significantly improve the reaction performance. To further understand the C-O bond hydrogenolysis process in the reaction, H_2O in the reaction was replaced by deuterated water (D_2O) and GC-MS was used to track deuterium and monitor hydrogen transfer during the reaction (the detailed MS spectra can be seen in Supplement). As shown in entry 1 of Scheme 2, no hydrogen/deuterium exchange between D_2O, acetophenone (120 m/z) and phenol (94 m/z) could be observed under this mild reaction

conditions (Figure S6). Entry 2 confirms that the solvent acetonitrile without hydrogen-donating ability does not provide hydrogen equivalents in this reaction (Figure S6) [9,49]. Finally, entry 3 shows that deuterated acetophenone (121 m/z) arises from the reaction with the deuterium label located at its methyl group based on MS spectrum, which clearly indicates that water was the origin for the C_β hydrogenation reaction after C_β-O bond cleavage (Figure S7, the peak at 43 m/z and 44 m/z are attributed to the summary of O=C-CH3(CH2D): 16+12+12+3(4)=43/44 (m/z); and the peak at 28 m/z and 27 m/z are attributed to the summary of C-CH3(CH2D): 12+12+3(4)=27/28 (m/z).) [50]. Moreover, it should be noticed that the hydrogen in the hydroxyl group of phenol is not deuterium after C-O cleavage and hydrogenation. Since PP-ol itself was the only hydrogen (H) source in this case, this result also domonstrates that a self-hydrogen transfer process in the reaction occurs, which is in line with previously reported work [9].

Kinetic isotope effect (KIE) experiments were performed with D_2O to probe the participation of water in this reaction and show that the reaction rate is reduced significantly when D_2O was present and a normal KIE value of $k(H_2O)/k(D_2O) \approx 1.52$ was obtained (Figure S8 in Supplement). These results indicate that the water is directly involved in this reaction and that the kinetics of hydrogenation using H_2O was faster than that of D_2O [50–52]. In contrast to the normal KIE result in this study, the hydrogenation of an sp^2C to an sp^3C has been reported to have an inverse KIE [53–55]. Therefore, the normal KIE result could be caused by faster O-H cleavage of H_2O, suggesting that the dissociation of O-H bond of water which provides proton to C-O bond hydrogenolysis process could be a critical step to this reaction [50,51,56].

21
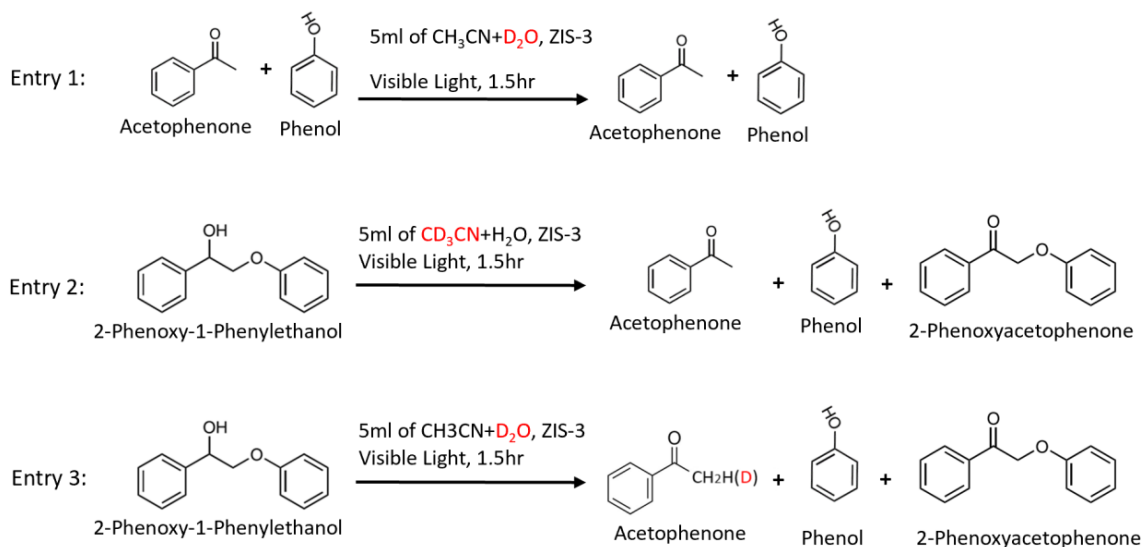
Scheme 2. Investigation of Hydrogenation and Hydrogen Transfer in the Reaction.

A variety of mechanisms on β-O-4 bond fragmentation via photocatalysis have been proposed previously and differ on the initial oxidative conversion by photogenerated holes. In some examples, the C_α−OH is oxidized firstly to the ketone C_α=O followed by decomposition to corresponding aromatic monomers with the assistance of photogenerated electrons [18,39]. This is evident, when PP-one is detected as an intermediate product which then decomposes to acetophenone and phenol. In these cases, the bond dissociation energy (BDE) of target C_β-O bonds can be reduced by the transformation of C-OH to C=O based on the theoretical calculations [37–39]. In contrast, the oxidative transformation of PP-ol to PP-one in this study is a side reaction as no conversion to aromatic monomers is seen when PP-one is used as reactant under catalytic conditions. An alternative mechanism in literature describes that the hydroxyl group or hydrogen on C_α is firstly oxidized by photogenerated holes via hydrogen-atom abstraction (HAA) process to form a radical which subsequently undergoes C_β-O bond cleavage and decomposition to the aromatic monomers with very high selectivity through reduction by photogenerated electrons [19–21,37]. In this study, it was seen that the introduction of 5,5-dimethyl-1-pyrroline-N-oxide (DMPO) as a radial scavenger (Entry 4, Table 4) caused the conversion of PP-ol to

22

be significantly suppressed along with a reduction in the selectivity for phenol and acetophenone. This result supports the radical intermediate mechanism proposed in the previous work and the radical intermediates converted from PP-ol are critical to the following C-O cleavage reaction [9,20,21,57].
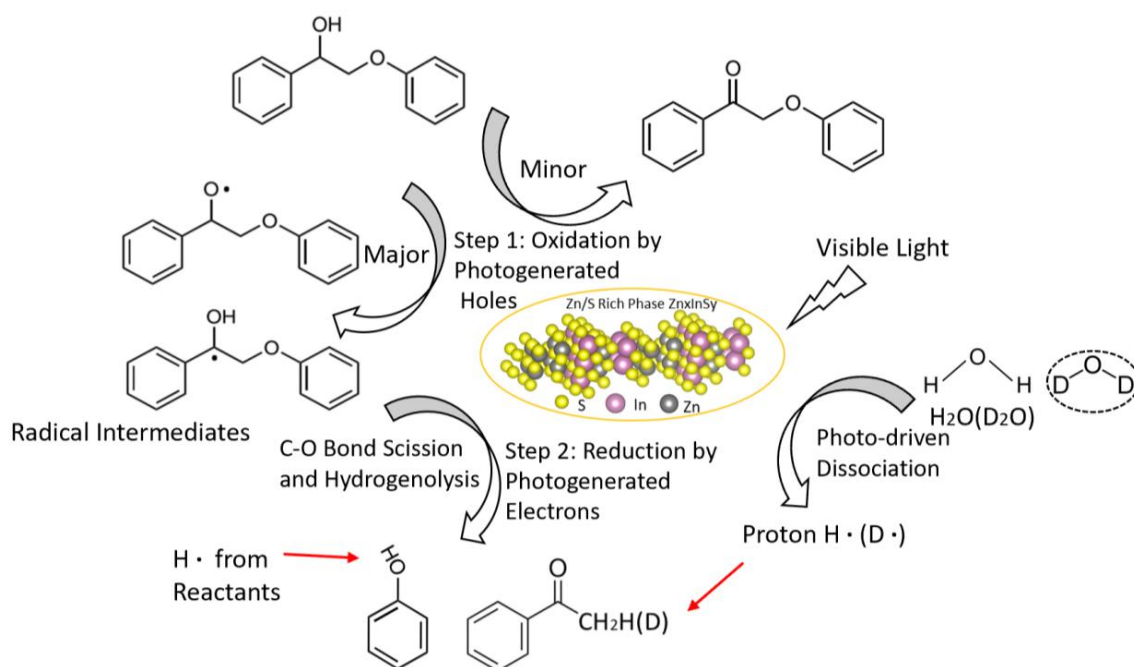
Scheme 3. Schematic Representation of Simultaneous Oxidative Hydrogen-Atom Abstraction (HAA) and Reductive Cleavage of the β-O-4 Bond via Radical Intermediate Pathway

As such, a plausible mechanism of photocatalytic C_β-O bond cleavage of PP-ol using zinc and sulfur rich phase zinc indium sulfide (ZIS-3) in the presence of water is proposed in Scheme 3. Upon the illumination of visible light, the photocatalyst is excited and generates both holes and electrons involving in this reaction. It should be noted that the separation efficiency and redox potentials of photogenerated charge carriers are enhanced by the additional Zn and S components in the zinc indium sulfide, thereby, resulting in better photocatalytic activity [58,59]. The photogenerated holes (minimum oxidation potential of 1.75 eV for ZIS-3) are strong enough to oxidize and drive hydrogen-atom abstraction (HAA) from Cα-OH (>1.44 eV) and benzylic Cα-H (>1.7 eV) in PP-ol, and thus will transform PP-ol to the radical intermediates (Step 1, major) and PP-one (Step 1, minor) via photo-oxidation process [9,10,21,59,60]. Based on the result of quenching experiments that the conversion of PP-ol significantly decreased with hole scavengers and radical scavengers in the reaction system, step

23

1 is very important to the following C-O bond fragmentation. However, the oxidation of PP-ol to by-product PP-one is a competing side reaction as PP-one cannot be converted to aromatic monomers. In this work, it is found that this competing side reaction is driven by photogenerated holes and can be suppressed by increasing water content in the reaction system. It is because water can consume redundant photogenerated holes thus suppresses the formation of ketone (C=O) [62]. In addition, it is reported that oxidization of water by photogenerated holes can generate protons for the following hydrogenation in step 2 [50,56,62,63]. Subsequently, the fragmentation and hydrogenolysis of C_β-O bonds in the radical intermediates can occur with the assistance of photogenerated electrons (step 2). During the hydrogenolysis of C-O bonds, it should be noted that acetophenone could be eventually formed through hydrogenation with the hydrogen derived from water. Simultaneously, the residual hydrogen from either $C\alpha$-OH or $C\alpha$-H in radical intermediates could be abstracted, then couple with the oxygen of phenoxy radical and form the hydroxyl group of phenol [9]. In summary, this study indicates that hydrogen derived from water can participate the hydrogenolysis of C-O bonds via photocatalysis and introducing water in the reaction system can promote the cleavage of C-O bonds in lignin model compound.

Conclusions

In this work, a series of zinc indium sulfide (ZIS) photocatalysts with controllable compositions have been successfully fabricated via a simple one-pot hydrothermal synthesis method. The characterization results show that the rich composition of zinc and sulfur in ZIS can boost the separation of photo-charge carriers and improve the oxidation and reduction properties. Among these, ZIS-3 which contains an optimized zinc and sulfur ratio exhibited a significantly enhanced photocatalytic performance for converting lignin model compounds and lignin biomass to valuable aromatic monomers by selectively cleaving C-O linkages between aromatic units under visible light irradiation. Also, different from previous studies in this area which required hydrogen gas, alcohols or other hydrogen sources still based on fossil feedstocks, water was used as a sustainable hydrogen origin in this work and can promote both conversion rate and selectivity for producing aromatic monomers. The mechanism studies of lignin model compound depolymerization reveal that radical intermediates are firstly formed by photo-

24

oxidation and followed by the hydrogenolysis of C-O bonds with hydrogen derived from water eventually transferred to the methyl group of single aromatic products. In summary, this study offers a great potential solution for valorization of abundant lignin biomass with sustainable hydrogen donor of water.

Acknowledgments

25

Reference

[1]   L. Jiang, H. Guo, C. Li, P. Zhou, Z. Zhang, Selective cleavage of lignin and lignin model compounds without external hydrogen, catalyzed by heterogeneous nickel catalysts, Chem. Sci. 10 (2019) 4458–4468. https://doi.org/10.1039/c9sc00691e.

[2]   J.C. Colmenares, R. Luque, Heterogeneous photocatalytic nanomaterials: Prospects and challenges in selective transformations of biomass-derived compounds, Chem. Soc. Rev. 43 (2014) 765–778. https://doi.org/10.1039/c3cs60262a.

[3]   A.J. Ragauskas, G.T. Beckham, M.J. Biddy, R. Chandra, F. Chen, M.F. Davis, B.H. Davison, R.A. Dixon, P. Gilna, M. Keller, P. Langan, A.K. Naskar, J.N. Saddler, T.J. Tschaplinski, G.A. Tuskan, C.E. Wyman, Lignin valorization: Improving lignin processing in the biorefinery, Science (80-.). 344 (2014). https://doi.org/10.1126/science.1246843.

[4]   M.M. Abu-Omar, K. Barta, G.T. Beckham, J.S. Luterbacher, J. Ralph, R. Rinaldi, Y. Román-Leshkov, J.S.M. Samec, B.F. Sels, F. Wang, Guidelines for performing lignin-first biorefining, Energy Environ. Sci. 14 (2021) 262–292. https://doi.org/10.1039/d0ee02870c.

[5]   X. Wu, X. Fan, S. Xie, J. Lin, J. Cheng, Q. Zhang, L. Chen, Y. Wang, Solar energy-driven lignin-first approach to full utilization of lignocellulosic biomass under mild conditions, Nat. Catal. 1 (2018) 772–780. https://doi.org/10.1038/s41929-018-0148-8.

[6]   C. Zhang, H. Li, J. Lu, X. Zhang, K.E. Macarthur, M. Heggen, F. Wang, Promoting Lignin Depolymerization and Restraining the Condensation via an Oxidation-Hydrogenation Strategy, ACS Catal. 7 (2017) 3419–3429. https://doi.org/10.1021/acscatal.7b00148.

[7]   S. Li, S. Kim, A.H. Davis, J. Zhuang, E.W. Shuler, D. Willinger, J. Lee, W. Zheng, B.D. Sherman, C.G. Yoo, G. Leem, Photocatalytic Chemoselective C − C Bond Cleavage at Room Temperature in Dye-Sensitized Photoelectrochemical Cells, ACS Catal. (2021). https://doi.org/10.1021/acscatal.1c00198.

[8]   S. Gazi, Valorization of wood biomass-lignin via selective bond scission: A minireview, Appl. Catal. B Environ. 257 (2019) 117936. https://doi.org/10.1016/j.apcatb.2019.117936.

[9]   N. Luo, M. Wang, H. Li, J. Zhang, T. Hou, H. Chen, X. Zhang, J. Lu, F. Wang, Visible-Light-Driven Self-Hydrogen Transfer Hydrogenolysis of Lignin Models and Extracts into Phenolic Products, ACS Catal. 7 (2017) 4571–4580. https://doi.org/10.1021/acscatal.7b01043.

[10]   X. Wu, X. Fan, S. Xie, J. Lin, J. Cheng, Q. Zhang, L. Chen, Y. Wang, Solar energy-driven lignin-first approach to full utilization of lignocellulosic biomass under mild conditions, Nat. Catal. 1 (2018) 772–780. https://doi.org/10.1038/s41929-018-0148-8.

[11]   M. Zaheer, R. Kempe, Catalytic hydrogenolysis of aryl ethers: A key step in lignin valorization to valuable chemicals, ACS Catal. 5 (2015) 1675–1684. https://doi.org/10.1021/cs501498f.

[12]   A. Shivhare, D. Jampaiah, S.K. Bhargava, A.F. Lee, R. Srivastava, K. Wilson, Hydrogenolysis of Lignin-Derived Aromatic Ethers over Heterogeneous Catalysts, ACS Sustain. Chem. Eng. (2021). https://doi.org/10.1021/acssuschemeng.0c06715.

[13]   K. Taniguchi, H. Nanao, O. Sato, A. Yamaguchi, M. Shirai, Solvolysis of benzyl phenyl ether in high-temperature aqueous methanol solution under high-pressure carbon dioxide, Green Chem. (2021). https://doi.org/10.1039/d0gc04008h.

[14]   J. Ji, H. Guo, C. Li, Z. Qi, B. Zhang, T. Dai, M. Jiang, C. Ren, A. Wang, T. Zhang, Tungsten-Based Bimetallic Catalysts for Selective Cleavage of Lignin C−O Bonds, ChemCatChem. 10 (2018) 415–421. https://doi.org/10.1002/cctc.201701240.

[15]   X. Wu, N. Luo, S. Xie, H. Zhang, Q. Zhang, F. Wang, Y. Wang, Photocatalytic transformations of lignocellulosic biomass into chemicals, Chem. Soc. Rev. 49 (2020) 6115–6516. https://doi.org/10.1039/d0cs00314j.

[16]   V. Molinari, G. Clavel, M. Graglia, M. Antonietti, D. Esposito, Mild Continuous Hydrogenolysis of Kraft Lignin over Titanium Nitride-Nickel Catalyst, ACS Catal. 6 (2016) 1663−1670. https://doi.org/10.1021/acscatal.5b01926.

[17]   N. Luo, M. Wang, H. Li, J. Zhang, H. Liu, F. Wang, Photocatalytic Oxidation-Hydrogenolysis of Lignin β-O-4 Models via a Dual Light Wavelength Switching Strategy, ACS Catal. 6 (2016)

27

7716–7721. https://doi.org/10.1021/acscatal.6b02212.

[18] G. Han, T. Yan, W. Zhang, Y.C. Zhang, D.Y. Lee, Z. Cao, Y. Sun, Highly Selective
      Photocatalytic Valorization of Lignin Model Compounds Using Ultrathin Metal/CdS, ACS
      Catal. 9 (2019) 11341–11349. https://doi.org/10.1021/acscatal.9b02842.

[19] X. Wu, S. Xie, C. Liu, C. Zhou, J. Lin, J. Kang, Q. Zhang, Z. Wang, Y. Wang, Ligand-
      Controlled Photocatalysis of CdS Quantum Dots for Lignin Valorization under Visible Light,
      ACS Catal. 9 (2019) 8443–8451. https://doi.org/10.1021/acscatal.9b02171.

[20] H. Yoo, M. Lee, S. Lee, J. Lee, S. Cho, H. Lee, H.G. Cha, H.S. Kim, Enhancing Photocatalytic
      β‐O‐4 Bond Cleavage in Lignin Model Compounds by Silver-Exchanged Cadmium
      Sulfide, ACS Catal. 10 (2020) 8465–8475. https://doi.org/10.1021/acscatal.0c01915.

[21] J. Lin, X. Wu, S. Xie, L. Chen, Q. Zhang, W. Deng, Y. Wang, Visible-Light-Driven Cleavage
      of C−O Linkage for Lignin Valorization to Functionalized Aromatics, ChemSusChem. 12
      (2019) 5023–5031. https://doi.org/10.1002/cssc.201902355.

[22] X. Gou, F. Cheng, Y. Shi, L. Zhang, S. Peng, J. Chen, P. Shen, Shape-controlled synthesis of
      ternary chalcogenide ZnIn2S 4 and CuIn(S,Se)2 nano-/microstructures via facile solution
      route, J. Am. Chem. Soc. 128 (2006) 7222–7229. https://doi.org/10.1021/ja0580845.

[23] D. Yan, Y. Von Lim, G. Wang, Y. Shang, X.L. Li, D. Fang, M.E. Pam, S.A. Yang, Y. Wang,
      Y. Shi, H.Y. Yang, Unlocking Rapid and Robust Sodium Storage Performance of Zinc-Based
      Sulfide via Indium Incorporation, ACS Nano. 15 (2021) 8507–8516.
      https://doi.org/10.1021/acsnano.1c00131.

[24] X. Li, Y. Cheng, Q. Wu, J. Xu, Y. Wang, Synergistic effect of the rearranged sulfur vacancies
      and sulfur interstitials for 13-fold enhanced photocatalytic H2 production over defective
      Zn2In2S5 nanosheets, Appl. Catal. B Environ. 240 (2019) 270–276.
      https://doi.org/10.1016/j.apcatb.2018.09.008.

[25] Y. Wu, H. Wang, W. Tu, Y. Liu, S. Wu, Y.Z. Tan, J.W. Chew, Construction of hierarchical
      2D-2D Zn3In2S6/fluorinated polymeric carbon nitride nanosheets photocatalyst for boosting

photocatalytic degradation and hydrogen production performance, Appl. Catal. B Environ. 233

(2018) 58–69. https://doi.org/10.1016/j.apcatb.2018.03.105.

[26] S. Shen, L. Zhao, L. Guo, Cetyltrimethylammoniumbromide (CTAB)-assisted hydrothermal

synthesis of ZnIn2S4 as an efficient visible-light-driven photocatalyst for hydrogen

production, Int. J. Hydrogen Energy. 33 (2008) 4501–4510.

https://doi.org/10.1016/j.ijhydene.2008.05.043.

[27] X. Shi, L. Mao, P. Yang, H. Zheng, M. Fujitsuka, J. Zhang, T. Majima, Ultrathin ZnIn2S4

nanosheets with active (110) facet exposure and efficient charge separation for cocatalyst free

photocatalytic hydrogen evolution, Appl. Catal. B Environ. 265 (2020) 118616.

https://doi.org/10.1016/j.apcatb.2020.118616.

[28] K. Wang, J. Fu, Y. Zheng, Insights into photocatalytic CO2 reduction on C3N4: Strategy of

simultaneous B, K co-doping and enhancement by N vacancies, Appl. Catal. B Environ. 254

(2019) 270–282. https://doi.org/10.1016/j.apcatb.2019.05.002.

[29] K. Wang, J. Lu, Y. Lu, C.H. Lau, Y. Zheng, X. Fan, Unravelling the C–C coupling in CO2

photocatalytic reduction with H2O on Au/TiO2-x: Combination of plasmonic excitation and

oxygen vacancy, Appl. Catal. B Environ. 292 (2021) 120147.

https://doi.org/10.1016/j.apcatb.2021.120147.

[30] X. Wang, X. Wang, J. Huang, S. Li, A. Meng, Z. Li, Interfacial chemical bond and internal

electric field modulated Z-scheme Sv-ZnIn2S4/MoSe2 photocatalyst for efficient hydrogen

evolution, Nat. Commun. 12 (2021) 1–11. https://doi.org/10.1038/s41467-021-24511-z.

[31] M. Hao, X. Deng, L. Xu, Z. Li, Noble metal Free MoS2/ZnIn2S4 nanocomposite for

acceptorless photocatalytic semi-dehydrogenation of 1,2,3,4-tetrahydroisoquinoline to produce

3,4-dihydroisoquinoline, Appl. Catal. B Environ. 252 (2019) 18–23.

https://doi.org/10.1016/j.apcatb.2019.04.002.

[32] F. Deng, F. Zhong, D. Lin, L. Zhao, Y. Liu, J. Huang, X. Luo, S. Luo, D.D. Dionysiou, One-

step hydrothermal fabrication of visible-light-responsive AgInS2/SnIn4S8 heterojunction for

29

highly-efficient photocatalytic treatment of organic pollutants and real pharmaceutical industry wastewater, Appl. Catal. B Environ. 219 (2017) 163–172. https://doi.org/10.1016/j.apcatb.2017.07.051.

[33]   Z. Zhang, L. Huang, J. Zhang, F. Wang, Y. Xie, X. Shang, Y. Gu, H. Zhao, X. Wang, In situ constructing interfacial contact MoS2/ZnIn2S4 heterostructure for enhancing solar photocatalytic hydrogen evolution, Appl. Catal. B Environ. 233 (2018) 112–119. https://doi.org/10.1016/j.apcatb.2018.04.006.

[34]   X. Ye, Y. Chen, Y. Wu, X. Zhang, X. Wang, S. Chen, Constructing a system for effective utilization of photogenerated electrons and holes: Photocatalytic selective transformation of aromatic alcohols to aromatic aldehydes and hydrogen evolution over Zn3In2S6 photocatalysts, Appl. Catal. B Environ. 242 (2019) 302–311. https://doi.org/10.1016/j.apcatb.2018.10.004.

[35]   Z. Xiang, W. Han, J. Deng, W. Zhu, Y. Zhang, H. Wang, Photocatalytic Conversion of Lignin into Chemicals and Fuels, ChemSusChem. 13 (2020) 4199–4213. https://doi.org/10.1002/cssc.202000601.

[36]   X. Liu, X. Duan, W. Wei, S. Wang, B.-J. Ni, Photocatalytic conversion of lignocellulosic biomass to valuable products, Green Chem. (2019) 4266–4289. https://doi.org/10.1039/c9gc01728c.

[37]   X. Wu, X. Fan, S. Xie, J. Lin, J. Cheng, Q. Zhang, L. Chen, Y. Wang, Solar energy-driven lignin-first approach to full utilization of lignocellulosic biomass under mild conditions, Nat. Catal. 1 (2018) 772–780. https://doi.org/10.1038/s41929-018-0148-8.

[38]   J.D. Nguyen, B.S. Matsuura, C.R.J. Stephenson, A photochemical strategy for lignin degradation at room temperature, J. Am. Chem. Soc. 136 (2014) 1218–1221. https://doi.org/10.1021/ja4113462.

[39]   N. Luo, M. Wang, H. Li, J. Zhang, H. Liu, F. Wang, Photocatalytic Oxidation-Hydrogenolysis of Lignin β-O-4 Models via a Dual Light Wavelength Switching Strategy, ACS Catal. 6 (2016)

30

7716–7721. https://doi.org/10.1021/acscatal.6b02212.

[40]   M.A. Barakat, J.M. Tseng, C.P. Huang, Hydrogen peroxide-assisted photocatalytic oxidation

of phenolic compounds, Appl. Catal. B Environ. 59 (2005) 99–104.

https://doi.org/10.1016/j.apcatb.2005.01.004.

[41]   J. Fang, P. Ye, M. Wang, D. Wu, A. Xu, X. Li, Hydrogenolysis and hydrogenation of β -O-4

ketones by a simple photocatalytic hydrogen transfer reaction, Catal. Commun. 107 (2018)

18–23. https://doi.org/10.1016/j.catcom.2018.01.005.

[42]   X. Cao, Z. Chen, R. Lin, W.C. Cheong, S. Liu, J. Zhang, Q. Peng, C. Chen, T. Han, X. Tong,

Y. Wang, R. Shen, W. Zhu, D. Wang, Y. Li, A photochromic composite with enhanced carrier

separation for the photocatalytic activation of benzylic C–H bonds in toluene, Nat. Catal. 1

(2018) 704–710. https://doi.org/10.1038/s41929-018-0128-z.

[43]   K. Su, H. Liu, B. Zeng, Z. Zhang, N. Luo, Z. Huang, Z. Gao, F. Wang, Visible-Light-Driven

Selective Oxidation of Toluene into Benzaldehyde over Nitrogen-Modified Nb2O5

Nanomeshes, ACS Catal. 10 (2020) 1324–1333. https://doi.org/10.1021/acscatal.9b04215.

[44]   Y.X. Tan, Z.M. Chai, B.H. Wang, S. Tian, X.X. Deng, Z.J. Bai, L. Chen, S. Shen, J.K. Guo,

M.Q. Cai, C.T. Au, S.F. Yin, Boosted Photocatalytic Oxidation of Toluene into Benzaldehyde

on CdIn2S4-CdS: Synergetic Effect of Compact Heterojunction and S-Vacancy, ACS Catal.

11 (2021) 2492–2503. https://doi.org/10.1021/acscatal.0c05703.

[45]   Y. Xu, L.Z. Zeng, Z.C. Fu, C. Li, Z. Yang, Y. Chen, W.F. Fu, Photocatalytic oxidation of

arylalcohols to aromatic aldehydes promoted by hydroxyl radicals over a CoP/CdS

photocatalyst in water with hydrogen evolution, Catal. Sci. Technol. 8 (2018) 2540–2545.

https://doi.org/10.1039/c8cy00138c.

[46]   Y. Pan, X. Yuan, L. Jiang, H. Yu, J. Zhang, H. Wang, R. Guan, G. Zeng, Recent advances in

synthesis, modification and photocatalytic applications of micro/nano-structured zinc indium

sulfide, Chem. Eng. J. 354 (2018) 407–431. https://doi.org/10.1016/j.cej.2018.08.028.

[47]   S. Shao, J. Yu, J.B. Love, X. Fan, An economic approach to produce iron doped TiO2

31

nanorods from ilmenite for photocatalytic applications, J. Alloys Compd. 858 (2021) 158388. https://doi.org/10.1016/j.jallcom.2020.158388.

[48] C. Jiang, H. Wang, Y. Wang, H. Ji, All solid-state Z‑ scheme CeO2/ZnIn2S4 hybrid for the photocatalytic selective oxidation of aromatic alcohols coupled with hydrogen evolution, Appl. Catal. B Environ. 277 (2020) 119235. https://doi.org/10.1016/j.apcatb.2020.119235.

[49] H. Chen, K. Wan, F. Zheng, Z. Zhang, Y. Zhang, D. Long, Mechanism insight into photocatalytic conversion of lignin for valuable chemicals and fuels production : A state-of-the-art review, Renew. Sustain. Energy Rev. 147 (2021) 111217. https://doi.org/10.1016/j.rser.2021.111217.

[50] Y. Wu, C. Liu, C. Wang, S. Lu, B. Zhang, Selective Transfer Semihydrogenation of Alkynes with H 2 O (D 2 O) as the H (D) Source over a Pd‑ P Cathode, Angew. Chemie. 132 (2020) 21356–21361. https://doi.org/10.1002/ange.202009757.

[51] H. Li, J. Shang, H. Zhu, Z. Yang, Z. Ai, L. Zhang, Oxygen Vacancy Structure Associated Photocatalytic Water Oxidation of BiOCl, ACS Catal. 6 (2016) 8276–8285. https://doi.org/10.1021/acscatal.6b02613.

[52] A. Das, I. Mandal, R. Venkatramani, J. Dasgupta, Ultrafast photoactivation of CH bonds inside water-soluble nanocages, Sci. Adv. 5 (2019) 1–14. https://doi.org/10.1126/sciadv.aav4806.

[53] Y. Wang, R. Qin, Y. Wang, J. Ren, W. Zhou, L. Li, J. Ming, W. Zhang, G. Fu, N. Zheng, Chemoselective Hydrogenation of Nitroaromatics at the Nanoscale Iron(III)–OH–Platinum Interface, Angew. Chemie - Int. Ed. 59 (2020) 12736–12740. https://doi.org/10.1002/anie.202003651.

[54] J. Shangguan, Y.H.C. Chin, Kinetic Significance of Proton-Electron Transfer during Condensed Phase Reduction of Carbonyls on Transition Metal Clusters, ACS Catal. 9 (2019) 1763–1778. https://doi.org/10.1021/acscatal.8b03470.

[55] K. Wang, M. Cao, J. Lu, Y. Lu, C.H. Lau, Y. Zheng, X. Fan, Operando DRIFTS-MS

investigation on plasmon-thermal coupling mechanism of CO2 hydrogenation on Au/TiO2: The enhanced generation of oxygen vacancies, Appl. Catal. B Environ. 296 (2021) 120341. https://doi.org/10.1016/j.apcatb.2021.120341.

[56]   S. Yu, P.K. Jain, Isotope Effects in Plasmonic Photosynthesis, Angew. Chemie. 132 (2020) 22666–22669. https://doi.org/10.1002/ange.202011805.

[57]   Y. Wang, Y. Liu, J. He, Y. Zhang, Redox-neutral photocatalytic strategy for selective C–C bond cleavage of lignin and lignin models via PCET process, Sci. Bull. 64 (2019) 1658–1666. https://doi.org/10.1016/j.scib.2019.09.003.

[58]   Q. Lin, Y.H. Li, M.Y. Qi, J.Y. Li, Z.R. Tang, M. Anpo, Y.M.A. Yamada, Y.J. Xu, Photoredox dual reaction for selective alcohol oxidation and hydrogen evolution over nickel surface-modified ZnIn2S4, Appl. Catal. B Environ. 271 (2020) 118946. https://doi.org/10.1016/j.apcatb.2020.118946.

[59]   Y.-J.X. Chang-Long Tan , Ming-Yu Qi , Zi-Rong Tang, Cocatalyst decorated ZnIn2S4 composites for cooperative alcohol conversion and H2 evolution, Appl. Catal. B Environ. 298 (2021). https://doi.org/10.1016/j.apcatb.2021.120541.

[60]   K. Qvortrup, D.A. Rankic, D.W.C. MacMillan, A general strategy for organocatalytic activation of c-h bonds via photoredox catalysis: Direct arylation of benzylic ethers, J. Am. Chem. Soc. 136 (2014) 626–629. https://doi.org/10.1021/ja411596q.

[61]   Z. Zhang, M. Wang, H. Zhou, F. Wang, Surface Sulfate Ion on CdS Catalyst Enhances Syngas Generation from Biopolyols, J. Am. Chem. Soc. 143 (2021) 6533–6541. https://doi.org/10.1021/jacs.1c00830.

[62]   D. Kong, Y. Zheng, M. Kobielusz, Y. Wang, Z. Bai, W. Macyk, X. Wang, J. Tang, Recent advances in visible light-driven water oxidation and reduction in suspension systems, Mater. Today. 21 (2018) 897–924. https://doi.org/10.1016/j.mattod.2018.04.009.

[63]   S.J.A. Moniz, S.A. Shevlin, D.J. Martin, Z.X. Guo, J. Tang, Visible-light driven heterojunction photocatalysts for water splitting-a critical review, Energy Environ. Sci. 8 (2015) 731–759.

33

1
2
3
4
5
6
7
8
9
10
11
12
13
14
15
16
17
18
19
20
21
22
23
24
25
26
27
28
29
30
31
32
33
34
35
36
37
38
39
40
41
42
43
44
45
46
47
48
49
50
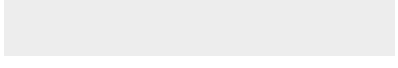51
52
53
54
55
56
57
58
59
60
61
62
63
64
65

34
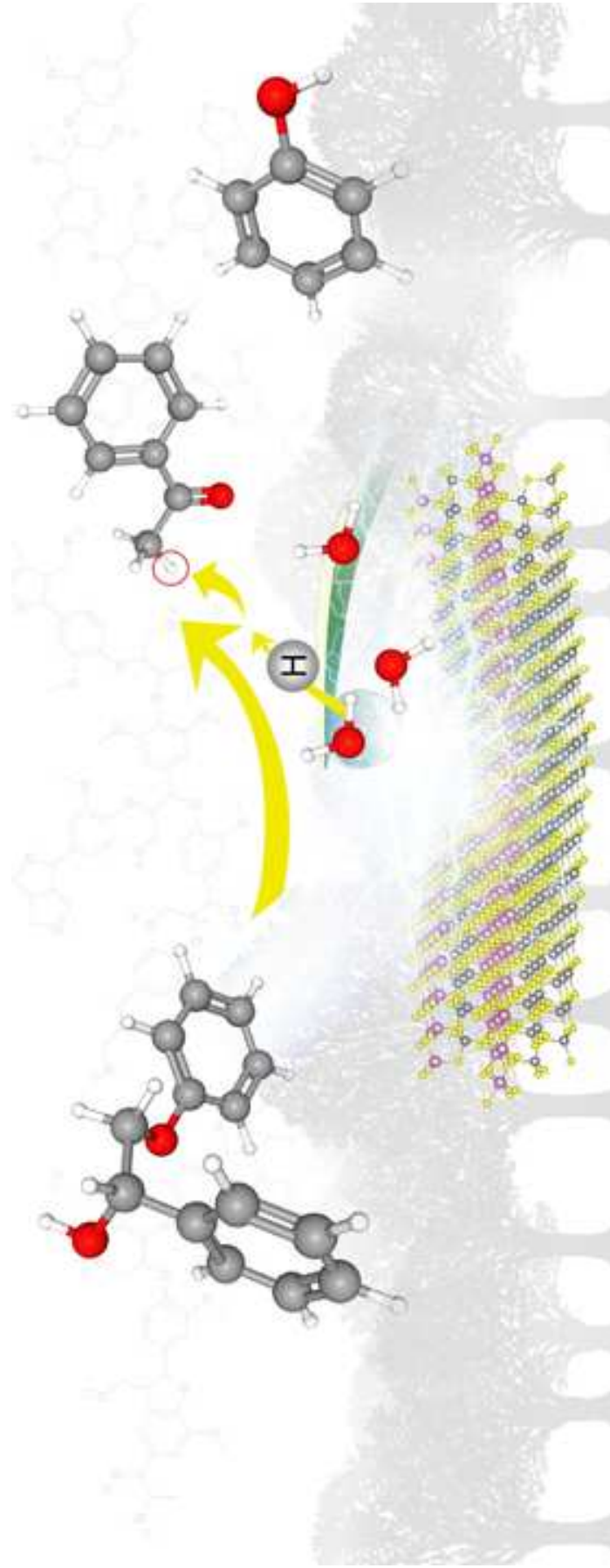
Highlights

- Completely conversion of lignin model compounds is achieved via photocatalysis
- Photocatalytic selective C_β-O cleavage leads to 90% selectivity of single aromatics
- H_2O acts as H donor and boosts the lignin model compound conversion to monomers
- Lignin biomass depolymerization to single aromatics can be driven by photocatalysis

Click here to access/download
Supplementary Material
Supply info.docx

CRediT author statement:

Shibo Shao: Conceptualization, Investigation, Validation, Formal analysis, Methodology, Visualization, Writing – Original Draft

Ke Wang: Investigation, Formal analysis, Methodology, Visualization, Writing - Review & Editing

Jason B. Love: Supervision, Resources, Writing - Review & Editing

Jialin Yu: Investigation, Formal analysis

Shangfeng Du: Investigation, Resources

Zongyang Yue: Investigation, Formal analysis

Xianfeng Fan: Conceptualization, Resources, Funding acquisition, Project administration, Supervision, Writing - Review & Editing

Declaration of interests

☒ The authors declare that they have no known competing financial interests or personal relationships that could have appeared to influence the work reported in this paper.

☐ The authors declare the following financial interests/personal relationships which may be considered as potential competing interests: